symmetry

MDPI

Article

Impact of Thermal Radiation on MHD GO-Fe_2O_4/EG Flow and Heat Transfer over a Moving Surface

Nur Aisyah Aminuddin [1,2], Nor Ain Azeany Mohd Nasir [2,*], Wasim Jamshed [3], Anuar Ishak [4], Ioan Pop [5] and Mohamed R. Eid [6,7]

1 Department of Defense Science, Faculty of Defense Science and Technology, Universiti Pertahanan Nasional Malaysia, Kem Sungai Besi, Kuala Lumpur 57000, Malaysia
2 Department of Mathematics, Centre for Defence Foundation Studies, Universiti Pertahanan Nasional Malaysia, Kem Sungai Besi, Kuala Lumpur 57000, Malaysia
3 Department of Mathematics, Capital University of Science and Technology (CUST), Islamabad 44000, Pakistan
4 Department of Mathematical Sciences, Faculty of Science and Technology, Universiti Kebangsaan Malaysia (UKM), Bangi 43600, Malaysia
5 Department of Mathematics, Babeş-Bolyai University, 400084 Cluj-Napoca, Romania
6 Department of Mathematics, Faculty of Science, New Valley University, Al-Kharga 72511, Al-Wadi Al-Gadid, Egypt
7 Department of Mathematics, Faculty of Science, Northern Border University, Arar 1321, Saudi Arabia
* Correspondence: norainazeany@upnm.edu.my

Highlights:

The stagnation point of heat transfer and hybrid nanofluid flow using the Powell-Eyring model toward stretching/shrinking surface problem is studied. The metal particles used are GO and Fe_2O_4 and Ethylene Glycol (EG) as base fluid. The analysis of entropy when the surface shrunk is highlighted. The thermal radiation and magnetic effects are also investigated.

Abstract: The heat transmission in a non-Newtonian hybrid nanofluid that combines particles of graphene oxide (GO) and iron dioxide (Fe_2O_4) with the base fluid chosen as ethylene glycol (EG) is analyzed, including the effects of radiation and magnetic influence. The hybrid nanofluid flow is assumed to be asymmetric because it flows along a horizontal shrinking surface in response to external inducements. The mathematically modelled partial differential equations (PDEs) form is then derived into ordinary differential equations (ODEs) by implementing a proper similarity transformation to the PDEs. The mathematical formulation is then algorithmically estimated employing the bvp4c solver in MATLAB. The parameters' effects on the skin friction measurement, local Nusselt number, entropy generation, velocity profile, and temperature profile are investigated and explained. This finding illustrated that the skin friction is augmented between 13.7% and 66.5% with the magnetic field, velocity slips, and the concentration of GO particles. As for the heat transmission ratio, only thermal radiation and velocity slip effects will affect the heat upsurge with the range of 99.8–147% for taken parameter values. The entropy for the shrinking case is found to increase between 16.6% and 43.9% with the magnetic field, velocity slip, and Eckert number.

Keywords: hybrid nanofluid; thermal radiation; magnetic field; entropy generation

check for updates

Citation: Aminuddin, N.A.; Nasir, N.A.A.M.; Jamshed, W.; Ishak, A.; Pop, I.; Eid, M.R. Impact of Thermal Radiation on MHD GO-Fe_2O_4/EG Flow and Heat Transfer over a Moving Surface. *Symmetry* **2023**, *15*, 584. https://doi.org/10.3390/sym15030584

Academic Editor: Rahmat Ellahi

Received: 27 January 2023
Revised: 13 February 2023
Accepted: 15 February 2023
Published: 23 February 2023

1. Introduction

Magnetohydrodynamics (MHD) is the study of the behavior and characteristics of magnetic-field-influenced electrically conducting liquid. Practical applications of MHD fluids can be seen in the plastic deformation process, the optical industry, power generators, etc. Ramzan et al. [1] ascertained the convective flow behavior of MHD hybrid nanofluid with velocity and thermal slips. Using an analytical method called the homotopy analysis technique, they discovered that an increase in magnetic field leads to a decrease in skin friction with or without velocity slip and an increase in magnetic field leads to a decrease in Nusselt number with or without thermal slip. Moreover, a higher magnetic field value will slow down the liquid's velocity because the magnetic field will create more friction. However, an appropriate magnetic field value will produce more Lorentz force, and more energy can be kept in the fluid, which will enhance the heat transfer. Hafeez et al. [2] explored the heat transference movement of a cross-nanofluid mixture on a contracting exterior. They discovered that the critical point of the magnetic effect elevated as the backward parameter raised from -1.2 to -1. Other scholars who also considered MHD flow on shrinking sheets were Othman et al. [3], Parvin et al. [4], and Lund et al. [5]. Moreover, it was shown that in the study by Yasir et al. [6] the MHD effect included in the stagnation point movement also intensifies the skin friction together with the Nusselt number. More studies about the MHD significance near the stagnation point at the shrinking slab were performed by Anuar et al. [7], Jawad et al. [8], and Rahman et al. [9].

One of the core components that influences heat transmission in fluid flow is known as Joule heating. When the electrical energy in a system turns into heat energy, the conversion itself is referred to as Joule heating. The purpose of lessening the value of current in the system is to reduce the destruction that may occur. With Joule heating, the conduction of electricity will be enhanced, which can help to improve heat transmission. As Joule heating has a massive repercussion against heat transmission, it is widely used in real-life applications, such as the petroleum and nuclear industry, electrical devices, chemical reactors, and microdevices and -systems. Using the Darcy–Forchheimer flow model to study non-Newtonian tangent hyperbolic fluid, Rao et al. [10] exposed that the Eckert number escalations increased the liquid's temperature, further diminishing the heat transmission efficiency. Venkatesan and Reddy [11] observed Al_2O_3/Blood fluid subject to Joule heating and other few impacts and concluded that the Hartmann number reduced the temperature of the fluid. Other previous papers that investigated Joule heating covering liquid movement were the exploration of Joule heating on MHD movement of Walters-B nanofluid close to extending slab, adopting the Runge–Kutta–Fehlberg technique by Gholinia et al. [12], Joule heating reactions in porous materials by Alaidrous and Eid [13], where they discussed electromagnetic radiative non-Newtonian nanofluid by optimal homotopy analytical method, Joule heating analysis of Cattaneo–Christov Heat Flux on CuO-Cu-Al_2O_3/H_2O flow over an inclined contracting plate by Jangid et al. [14], and the exploration of MHD bioconvection of nano liquid flow on an elongating wedge by Ferdows et al. [15].

Extensive literature has been developed on nanofluids, and a lot of researchers are gaining interest in hybrid nanofluids. Two different types of nanoparticles are combined to create hybrid nanofluids in the chosen base fluid. It is different from nanofluid as nanofluid only uses one type of nanoparticle. Recently, hybrid nanofluids have been actively used in many industrial applications, such as radiators, generators, and cooling systems. Previous studies have shown that hybrid nanofluids allow the heat exchange among the properties to be optimized and embellish the thermal conductivity by indirectly boosting the heat transmission effectiveness. Hybrid nanofluids are discovered to be less damaging to the environment and help to save energy. It can also help to lower the costs of individual nanoparticle, as only a smaller concentration is needed. It is stated that hybrid nanofluids can improve the suitability and practicality of conventional nanofluids. As the benefits are evident, it is crucial to discover more about heat transfer by utilizing hybrid nanofluids in different conditions. The study of nonlaminar flow of CuO/H_2O within a wavy microchannel [16] and the analysis of Ag/H_2O inside a duplex-layered sinusoidal heat sink [17] are some of the studies on conventional nanofluids. Qureshi [18] compared the proportion of heat transmission between ZrO_2–Cu/EO mixture nanofluid and ZrO_2-EO nanofluid. The outcomes of this investigation revealed that mixture nanofluid is a superior heat conductor compared to traditional nanofluid. Mashayekhi et al. [19] investigated Cu-Al_2O_3/H_2O within a binary-layered microchannel with heat absorption and found that the wall's structure affects the heat transmission rate significantly. Hussain et al. [20] did a study about the reaction and heat transfer on GO-MoS_2/H_2O hybrid nanofluid on a curved surface with shape factors. They found that shape factors have a more noticeable impact on a hybrid nanofluid. The involvement of GO was examined in [21] with the effect of radiation, and it was concluded that the concentration of GO augments the momentum and thermal effects of the liquid. Another research that studied GO hybrid nanofluid compares GO/EO and GO-Fe_3O_4 with thermal and magnetic effects [22]. Few other studies show the usage of Fe_2O_4 particles in heat transfer problems [23–25].

For a better understanding, Newtonian fluids follow Newton's law of viscosity, which means that they have a constant viscosity. Non-Newtonian fluids do not obey the law and have a changing viscosity. Numerous studies have investigated non-Newtonian fluids, and a lot of models are presented on this type of fluid with different thermophysical aspects. A study about non-Newtonian fluids reported that Casson fluid, Carreau fluid, Powell–Eyring fluid, and Prandtl–Eyring fluid are some non-Newtonian fluid models [26]. One of the applications of this fluid in the industry is in processing chemicals, hence attracting an increasing amount of scholars' attention. Powell–Eyring fluid is a model developed by Powell and Eyring [27]. Usually, it is very challenging to find the solution to non-Newtonian models due to their complex system equations. However, this model's simplicity helps researchers gain solutions for their problems more efficiently [28]. Previous studies that have emphasized this model are the entropy study of Powell–Eyring Cu-Al_2O_3/ethylene glycol fluid [29] and the effects of MHD and heat source/sink of Powell–Eyring fluid on a stretching surface [30]. One of the crucial components that is needed in the heat transfer process is the base fluid. However, using the conventional base fluid without adding nanoparticles gives poor thermal conductivity. As a result, the researchers started to add particles to the base fluids. Some fluids that are mainly used for this process are water, engine oil, kerosene oil, and ethylene glycol. A few studies on ethylene glycol as the base fluid have been completed earlier, such as MHD flow of Cu/EG nanofluid with heat generation/absorption effect [31], Cu-Fe3O4/EG-based hybrid nanofluid slip flow on the elongating surface [32], and the mixed convective flow of SWCNT-MWCNT/EG hybrid nanofluid [33].

The electromagnetic wave radiation that a surface emits due to its heat is known as thermal radiation. Some applications that benefit from thermal radiation are solar technology, nuclear plant, spacecraft aerodynamics, etc. Numerous scholars and experts are interested in examining the influence of radiation on fluids' behavior. The effect of thermal radiation on an MHD Powell–Eyring C71500-Ti_6Al_4V/$C_2H_6O_2$-H_2O was studied by Roja [34], where an increase in radiation led to an increase in entropy and decrease in the temperature of the liquid. Rashad et al. [35] looked into MHD Powell–Eyring Cu-Fe_3O_4/EG within a permeable medium. They detected that as the value of the magnetic field and radiation were enhanced, the rapidity of the fluid is improved, although the radiation effect alone enhanced the temperature within the boundary layer. Many scholars solved the problem of the radiation effect in heat transfer by studying the laminar flow of Cu/H_2O within an upright channel [36], MHD flow of Cu/H_2O between parallel plates [37], and MHD flow of GO/H_2O in a porous channel [38] for nanofluids and MHD flow of CuO-Al_2O_3/H_2O over two different geometries [39], MHD Al_2O_3-Ag/H_2O flow over a stretching sheet [40], and MHD Williamson MoS_2-ZnO/EG flow over a permeable stretching sheet [41] for hybrid nanofluids.

Entropy generation, associated with the second law of thermodynamics, is one of the interferences that occurs in the system. When operating a system in real-life scenarios, it is impossible to say that the system is in an ideal condition, where no energy, in the form of heat and friction, is wasted. Hence, the primary concern of many experts is to minimize the energy lost from the system. Entropy generation analysis is introduced to point out the irreversible loss that occurs in a thermal process and to calculate the system's disturbance, help assess the ability, and achieve maximum effectiveness of a system. There are many practical applications of entropy generation analysis, such as in electrical devices, the cooling and heating industry, and biological and chemical systems. The entropy generation of Cu-Al_2O_3/EG hybrid nanofluid through a rotating channel was analytically solved and has been reported that a stronger magnetic field leads to growth of entropy generation, as the magnetic field produces a lot of resistance creating more Joule heating in the system [42]. The radiation effect also increases entropy in the system because the higher intensity of radiation increases the temperature of the liquid. Similar results on the effect of magnetic and radiation intensities on the entropy of the system can be seen in [43]. The entropy of non–Newtonian Carreau hybrid nanofluid was studied in [44], and it was concluded that a hybrid nanoparticle system produces more entropy than one that uses only one nanomaterial. The study of entropy and curvature effect of Cu–Al_2O_3/Blood in [45] showed that a higher concentration of the nanoparticles generates higher entropy because a higher concentration increases the flow's momentum and enhances the randomness of the particles. They also stated that entropy in the system of hybrid nanofluid is high, while the entropy produced from only the base fluid system is lower. Entropy of hybrid nanofluids was further analyzed by Ghali et al. [46] and Hayat et al. [47].

Inspired by the previously discussed research and the vital elements of non-Newtonian hybrid nanofluid and entropy studies, this work focuses on MHD GO-Fe_2O_4/EG hybrid nanofluid's flow and heat transfer over the expanding and contracting surfaces with thermal radiation effect. Fe_2O_4 is widely used as a catalyst in the industry due to its magnetic behavior. Whereas, GO, used in many applications due to its characteristics, is a very promising particle to boost the catalyst. Hence, the combination of GO-Fe_3O_4 with ethylene glycol is promising for a thermal heating and cooling system with minimum residue left in the system for a solar battery, radiator, and device sensors with minimal cost. Several studies focus on stretching surfaces with entropy analysis, but only a little information is available when the surface shrinks with entropy analysis. The unstable boundary layer partial differential equations are converted into a system of ordinary differential equations using the proper similarity transformation. The collected results for velocity, temperature, skin friction coefficient, local Nusselt number, and entropy generation are reviewed and highlighted in tables and graphs.

2. Mathematical Modelling

Figure 1 demonstrates a steady, two-dimensional boundary layer flow into a moving horizontal plate. The surface is assumed to be shrunk with the velocity $U_w(x)$ along the $x-$path, and the mass flux constant velocity is denoted by v. The constant temperature of the flat plate is T_w and T_∞ is known as the ambient temperature. Hence, the boundary layer equations from these assumptions will be derived as (Source: Waini et al. [48] and Wasim et al. [49]).

$$\frac{\partial u}{\partial x} + \frac{\partial v}{\partial y} = 0 \tag{1}$$

$$u\frac{\partial u}{\partial x} + v\frac{\partial u}{\partial y} = u_e\frac{\partial u_e}{\partial x} + \left(\nu_{hnf} + \frac{1}{\rho_{hnf}\beta^*\varepsilon^3}\right)\frac{\partial^2 u}{\partial y^2} - \frac{1}{2\rho_{hnf}\beta^*\varepsilon^3}\left(\frac{\partial u}{\partial y}\right)^2\frac{\partial^2 u}{\partial y^2} - \frac{\sigma\, B_0^2}{\rho}\,(u-u_e) \tag{2}$$

$$u\frac{\partial T}{\partial x} + v\frac{\partial T}{\partial y} = \frac{k_{hnf}}{(\rho C_p)_{hnf}}\left(\frac{\partial^2 T}{\partial y^2}\right) + \frac{\mu_{hnf}}{(\rho C_p)_{hnf}}\left(\frac{\partial\, u}{\partial\, y}\right)^2 + \frac{\sigma\, B_0^2}{(\rho C_p)_{hnf}}(u-u_e)^2 - \frac{1}{(\rho C_p)_{hnf}}\left(\frac{\partial q_r}{\partial y}\right) \tag{3}$$

Subject to boundary conditions:

$$u = \alpha U_w + \epsilon_0\frac{\partial u}{\partial y},\; v = 0, -k_{hnf}\frac{\partial T}{\partial y} = h_f(T_w - T)\; at\; y = 0$$

$$u \to u_e,\; T \to T_\infty,\; as\; y \to \infty \tag{4}$$

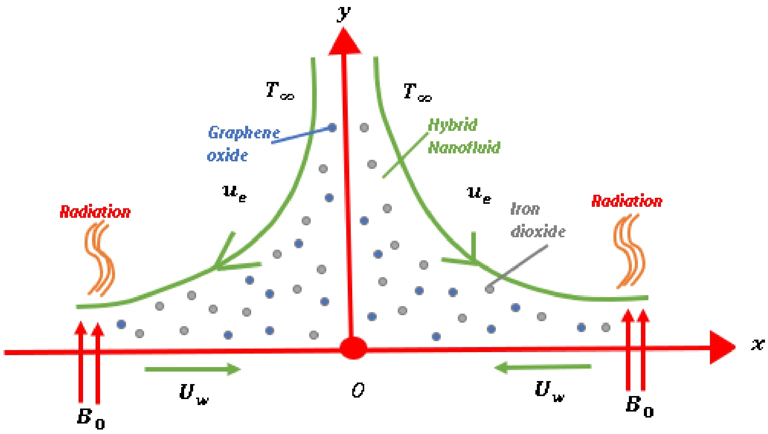

Figure 1. A shrinking surface model.

The solutions for Equations (1)–(3) along with the boundary condition (4) can be obtained by reducing to ordinary differential equations with the implementation of similarity transformation (Source: Waini et al. [48]), which is given as,

$$\psi(\eta) = \sqrt{b\nu_f} x f(\eta),\ \vartheta(\eta) = {}^{T-T_\infty}/_{T_w - T_\infty},\ \eta = \sqrt{{}^{b}/_{\upsilon_f}} y \tag{5}$$

and given that the stream function is denoted as ψ which is collaborated with the following equation

$$u = \frac{\partial \psi}{\partial y},\ v = -\frac{\partial \psi}{\partial x} \tag{6}$$

The reduced partial differential equations are

$$\left(\frac{1}{\phi_a \phi_b} + \chi \frac{1}{\phi_b}\right) f''' + f f'' - f'^2 - \frac{\chi \varsigma}{\phi_b} f''^2 f''' - M\left(f' - 1\right) + 1 = 0 \tag{7}$$

$$\frac{\phi_d}{Pr\phi_c}\left(1 + \frac{PrRd}{\phi_d}\right)\vartheta'' + Ec\frac{1}{\phi_c}\left[\frac{1}{\phi_a} f''^2 + M\left(f' - 1\right)^2\right] + f\vartheta' = 0 \tag{8}$$

with boundary conditions:

$$f'(0) = \alpha + \epsilon f'',\ f(0) = 0, -\frac{k_{hnf}}{k_f}\vartheta'(0) = Bi[1 - \vartheta(0)]$$

$$f'(\eta) \to 1,\ \vartheta(\eta) \to 0 \ as\ \eta \to \infty \tag{9}$$

Here the parameters involved are material parameter $\chi = \frac{1}{\mu_f \beta^* \varepsilon^3}$ and $\varsigma = \frac{b^3 x^2}{2\upsilon_f}$, magnetic parameter $M = \frac{\sigma B_0^2}{b\rho_f}$, radiation $Rd = \frac{16\sigma^* T_\infty^3}{\upsilon_f (\rho C_p)_f 3k^*}$, Prandtl number $Pr = \frac{\upsilon_f (\rho C_p)_f}{k_f}$, Eckert number $Ec = \frac{b^2 x^2}{(T_w - T_\infty)(C_p)_f}$, velocity slip $\epsilon = \epsilon_0 \sqrt{\frac{b}{\upsilon_f}}$, and Biot number $Bi = \frac{h_f}{k_f}\sqrt{\frac{\upsilon_f}{b}}$. α represents the stretching and shrinking parameter, in which $\alpha > 0$ implies the elongating region while $\alpha < 0$ indicates the contracting surface.

The hybrid nanofluid parameters (Source: Qureshi [18]) are denoted as follows,

$$\phi_a = (1 - \phi_1)^{2.5} (1 - \phi_2)^{2.5} = \frac{\mu_f}{\mu_{hnf}} \tag{10}$$

$$\phi_b = (1 - \phi_2)\left[(1 - \phi_1) + \phi_1 \frac{\rho_{s1}}{\rho_f}\right] + \phi_2 \frac{\rho_{s2}}{\rho_f} = \frac{\rho_{hnf}}{\rho_f} \tag{11}$$

$$\phi_c = (1-\phi_2)\left[(1-\phi_1)+\phi_1\frac{(\rho C_p)_{s1}}{(\rho C_p)_f}\right]+\phi_2\frac{(\rho C_p)_{s2}}{(\rho C_p)_f} = \frac{(\rho C_p)_{hnf}}{(\rho C_p)_f} \quad (12)$$

$$\phi_d = \frac{k_{hnf}}{k_f} \quad (13)$$

The formulas and values involved in calculating the hybrid nanofluid parameters in Equations (10)–(13) is given in Tables 1 and 2 respectively.

Table 1. The thermophysical features of hybrid nanofluids (Source: Devi and Devi et al. [50]).

Features	Hybrid Nanofluid
Density (ρ)	$\rho_{hnf} = (1-\phi_2)\left[(1-\phi_1)\rho_f + \phi_1\rho_{s1}\right] + \phi_2\rho_{s2}$
Viscosity (μ)	$\mu_{hnf} = \mu_f/(1-\phi_1)^{2.5}(1-\phi_2)^{2.5}$
Heat capacity (ρC_p)	$(\rho C_p)_{hnf} = (1-\phi_2)\left[(1-\phi_1)(\rho C_p)_f + \phi_1(\rho C_p)_{s1}\right] + \phi_2(\rho C_p)_{s2}$
Thermal conductivity (k)	$k_{hnf} = \frac{k_{s2}+2k_{nf}-2\phi_2(k_{nf}-k_{s2})}{k_{s2}+2k_{nf}+\phi_2(k_{nf}-k_{s2})} \times k_{nf}$ With $k_{nf} = \frac{k_{s1}+2k_f-2\phi_1(k_f-k_{s1})}{k_{s1}+2k_f+\phi_1(k_f-k_{s1})} \times k_f$

Table 2. The values of the thermophysical properties of nanoparticles and base fluid (Source: Hussain et al. [20], Muhammad et al. [23] and Ogunseye et al. [29]).

Thermophysical Properties	Graphene Oxide (GO)	Iron Dioxide (Fe_2O_4)	Ethylene Glycol (EG)
$k\ (Wm^{-1}K^{-1})$ Thermal conductivity	5000	9.7	0.253
$\rho\ (kgm^{-2})$ Density	1800	5180	1115
$C_p\,(Jkg^{-1}K^{-1})$ Specific heat	717	670	2430

The critical physical quantities for this mathematical modelling are the skin friction coefficient C_f, local Nusselt number Nu_x and entropy generation N_G. The formulation for these physical quantities is as follows (Source: Qureshi [18] and Wasim et al. [49]).

$$C_f = \frac{\tau_w}{\rho_f U_w^2},\ Nu_x = \frac{xq_w}{k_f(T_w - T_\infty)},\ N_G = \frac{T_\infty^2 a^2 E_G}{k_f(T_w - T_\infty)^2} \quad (14)$$

Along with the definition of the shear stress $\tau_w = \left[\left(\mu_{hnf} + \frac{1}{\beta^*\varepsilon^3}\right)\frac{\partial u}{\partial y} - \frac{1}{6\beta^*\varepsilon^3}\left(\frac{\partial u}{\partial y}\right)^3\right]_{y=0}$, the heat flux $q_w = k_{hnf}\left[1 + \frac{16\sigma^* T_\infty^3}{3k^* k_f}\right]\left(\frac{\partial T}{\partial y}\right)_{y=0}$ and $E_G = \frac{k_{hnf}}{T_\infty^2}\left[\left(\frac{\partial T}{\partial y}\right)^2 + \frac{16\sigma^* T_\infty^3}{3k^* k_f}\left(\frac{\partial T}{\partial y}\right)^2\right] + \frac{\mu_{hnf}}{T_\infty}\left(\frac{\partial u}{\partial y}\right)^2$.

By substituting Equation (6) in Equation (14), the following is obtained.

$$C_f Re_x^{\frac{1}{2}} = \left(\frac{1}{\phi_a} + \chi\right)f''(0) - \frac{\chi\varsigma}{3}(f''(0))^3,\ Nu_x Re_x^{-\frac{1}{2}} = -\phi_d(1+Rd)\theta'(0),$$

$$N_G Re^{-1} = \phi_d(1+Rd)(\theta'(0))^2 + \frac{B_r T_\infty}{\phi_a(T_w - T_\infty)}(f''(0))^2 \quad (15)$$

The notation for the above equation is given as $Re_x = x\frac{U_w}{v_f}$, which is denoted as a local Reynolds number while $Re = \frac{U_w b^2}{v_f x}$ is the Reynolds number, and the Brinkmann number is given as $B_r = \frac{\mu_f U_w^2}{k_f(T_w - T_\infty)}$.

3. Flow Stability

The similarity differential Equations (2) and (3) have identified several solutions. Thus, stability evaluation is necessary to determine which solutions can provide stability. The unstable forms for the similarity differential equations, where t denotes time, are

$$\frac{\partial u}{\partial t} + u\frac{\partial u}{\partial x} + v\frac{\partial u}{\partial y} = u_e\frac{\partial u_e}{\partial x} + \left(\nu_{hnf} + \frac{1}{\rho_{hnf}\beta^*\varepsilon^3}\right)\frac{\partial^2 u}{\partial y^2} - \frac{1}{2\rho_{hnf}\beta^*\varepsilon^3}\left(\frac{\partial u}{\partial y}\right)^2\frac{\partial^2 u}{\partial y^2} - \frac{\sigma B_0^2}{\rho_f}(u - u_e) \tag{16}$$

$$\frac{\partial T}{\partial t} + u\frac{\partial T}{\partial x} + v\frac{\partial T}{\partial y} = \frac{k_{hnf}}{(\rho C_p)_{hnf}}\left(\frac{\partial^2 T}{\partial y^2}\right) + \frac{\mu_{hnf}}{(\rho C_p)_{hnf}}\left(\frac{\partial u}{\partial y}\right)^2 + \frac{\sigma B_0^2}{(\rho C_p)_{hnf}}(u - u_e)^2 - \frac{1}{(\rho C_p)_{hnf}}\left(\frac{\partial q_r}{\partial y}\right) \tag{17}$$

τ is a new variable that denotes the dimensionless time variable. Therefore, the similarity variables (Source: Khashi'ie et al. [51]) create dimensionless unsteady equations:

$$\psi = \sqrt{b\nu_f}\,xf(\eta,\tau),\ \eta = \sqrt{\frac{b}{v_f}}y,\ \vartheta(\eta,\tau) = T - T_\infty/T_w - T_\infty$$

$$u = axf'(\eta,\tau),\ v = -\sqrt{a\nu_f}f\ as\ \tau = at \tag{18}$$

The updated differential Equations (16) and (17) are reduced to

$$\left(\frac{\partial f}{\partial \eta}\right)^2 - f\frac{\partial^2 f}{\partial^2 \eta} = 1 + \left(\frac{1}{\phi_a\phi_b} + \chi\frac{1}{\phi_b}\right)\frac{\partial^3 f}{\partial \eta^3} - \frac{\chi\varsigma}{\phi_b}\left(\frac{\partial^2 f}{\partial^2 \eta}\right)^2\frac{\partial^3 f}{\partial \eta^3} - M\left(\frac{\partial f}{\partial \eta} - 1\right) - \frac{\partial^2 f}{\partial \tau \partial \eta} \tag{19}$$

$$\frac{\phi_d}{Pr\phi_c}\left(1 + \frac{PrRd}{\phi_d}\right)\frac{\partial^2 \vartheta}{\partial \eta^2} + Ec\frac{1}{\phi_c}\left[\frac{1}{\phi_a}\left(\frac{\partial^2 f}{\partial^2 \eta}\right)^2 + M\left(\frac{\partial f}{\partial \eta} - 1\right)^2\right] + f\frac{\partial \vartheta}{\partial \eta} - \frac{\partial \vartheta}{\partial \tau} = 0 \tag{20}$$

with the boundary conditions:

$$f'(0,\tau) = \alpha + \epsilon f'',\ f(0,\tau) = 0\,, -\frac{k_{hnf}}{k_f}\vartheta'(0,\tau) = Bi[1 - \vartheta(0,\tau)]$$

$$f'(\eta,\tau) \to 1,\ \vartheta(\eta,\tau) \to 0\ as\ \eta \to \infty \tag{21}$$

To determine the stability of both solutions $f(\eta) = f_0(\eta)$ and $\vartheta(\eta) = \vartheta_0(\eta)$, $f(\eta,\tau)$ and $\vartheta(\eta,\tau)$ are introduced (Source: Khashi'ie et al. [51]):

$$f(\eta,\tau) = f_0(\eta) + e^{-\gamma\tau}F(\eta,\tau),\ \vartheta(\eta,\tau) = \vartheta_0(\eta) + e^{-\gamma\tau}G(\eta,\tau) \tag{22}$$

It should be highlighted that $F(\eta,\tau)\ and\ G(\eta,\tau)$ are small in comparison to $f_0(\eta)$ and $\vartheta_0(\eta)$, respectively, since variable γ is known as an unknown eigenvalue. When Equation (22) is substituted into Equations (19)–(21), the linearized eigenvalue equations are

$$\left(\frac{1}{\phi_a\phi_b} + \chi\frac{1}{\phi_b}\right)\frac{\partial^3 F}{\partial \eta^3} - \frac{\chi\varsigma}{\phi_b}\left(f_0''^2\frac{\partial^3 F}{\partial \eta^3} + 2f_0''f_0'''\frac{\partial^2 F}{\partial \eta^2}\right) + f_0\frac{\partial^2 F}{\partial \eta^2} - (2f_0' + M - \gamma)\frac{\partial F}{\partial \eta} + Ff_0'' - \frac{\partial^2 F}{\partial \eta \partial \tau} = 0 \tag{23}$$

$$\frac{\phi_d}{Pr\phi_c}\left[1 + \frac{PrRd}{\phi_d}\right]\frac{\partial^2 G}{\partial \eta^2} + (f_0(\eta) + \gamma)\frac{\partial G}{\partial \eta} + \frac{Ec}{\phi_c}\left[\frac{2}{\phi_a}f_0''(\eta)\frac{\partial^2 F}{\partial \eta^2} + 2M(f_0'(\eta) - 1)\frac{\partial F}{\partial \eta}\right] + F(\eta,\tau)\vartheta_0'(\eta) - \frac{\partial G}{\partial \tau} = 0 \tag{24}$$

The boundary conditions are

$$\frac{\partial}{\partial\eta}F(0,\tau) = \epsilon\frac{\partial^2}{\partial\eta^2}F(0,\tau),\ F(0,\tau) = 0,\ \frac{\partial}{\partial\eta}G(0,\tau) = BiG(0,\tau)\frac{k_f}{k_{hnf}}$$

$$\frac{\partial}{\partial\eta}F(\eta,\tau) \to 0,\ G(\eta,\tau) \to 0\ as\ \eta \to \infty \tag{25}$$

The potential range of the eigenvalues $\gamma_1 < \gamma_2 < \gamma_3 < \cdots$ can be determined by easing the boundary condition $F(\infty) = 0$ or $G(\infty) = 0$. In this paper, the boundary condition $F'(\eta) \to 0$ is relaxed and substituted by initial condition $F''(0) = 1$. γ_1 is the smallest eigenvalue, and it serves as the stability determinant. When the value of γ_1 is less than zero, it portrays that there is a formation of disturbance in the solution; hence, the computed solution is unstable. On the other hand, when the value of γ_1 is more than zero, it explains that the computed solution is stable with the deterioration of disturbance. The smallest eigenvalues at every specific spot are illustrated in Figure 2. It shows that the stable solution is the upper branch solution since the value is in the positive range, while the lower branch solution is the unstable solution.

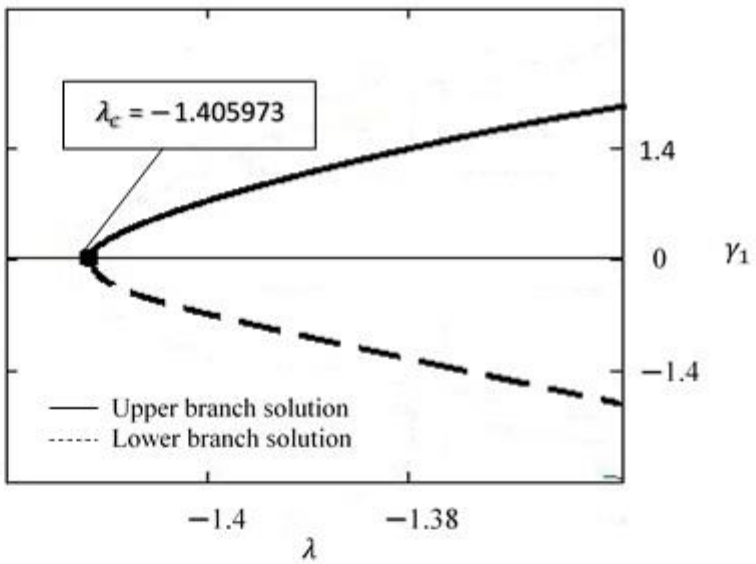

Figure 2. Stability analysis for Equations (23)–(25).

4. Results and Discussion

Many solvers can be used to solve Equations (7)–(9) by implementing shooting techniques to cater for the solutions for boundary value problems. For instance, the Runge–Kutta–Fehlberg-45 (RKF-45) method combined with the shooting technique is used to solve the boundary value problems as in [52]. Likewise, Al-Mubaddel et al. [53] used bvp4c, which employs the three-stage Lobatto IIIa formula to solve the boundary value problems. Using bvp4c solver built-in MATLAB, Equations (7)–(9) are computed. The bvp4c solver is preferred mostly because it is a favorable solver that can untangle PDEs with complicated boundary conditions. It is also easier to compute the solution for shrinking surface cases. Some former works that have used this solver can be found in [6,14,15]. Provided multiple parameters, which are M, R, Ec, ϵ, and Bi, a relevant discussion is held. The Prandtl number for the base fluid, ethylene glycol, is set to be $Pr = 204$ (see Ganesh et al. [54]). In this paper, ϕ_1 indicates Fe_2O_4 nanoparticles and ϕ_2 represents GO nanoparticles. The concentration for both particles is 0.01.

Validation is essential to ensure the reliability of this paper. That is, to compare recent discoveries and earlier findings from past researchers by numerical computing. A numerical comparison with Bachok et al. [55] and Wahid et al. [56] is used to verify the accuracy of the present model. Table 3 presents the comparison data that we obtained, and it is shown that the data are all within the acceptable range. Hence, it is satisfactory to assume that the results are reliable.

Table 3. Comparison of skin friction coefficient when $f''(0)$ and $M = Ec = 0$.

α	Bachok et al. [55]		Wahid et al. [56]		Present Study	
	1st Solution	**2nd Solution**	**1st Solution**	**2nd Solution**	**1st Solution**	**2nd Solution**
−0.25	1.4022408	-	1.402240767	-	1.402240774	-
−0.5	1.4956698	-	1.495669720	-	1.495669732	-
−0.75	1.4892983	-	1.489298191	-	1.489298195	-
−1.15	1.0822315	0.1167022	1.082231123	0.116702139	1.082231123	0.116702132
−1.2	0.9324739	0.2336497	0.932473307	0.233649729	0.932473309	0.233649727
−1.2465	0.5842956	0.5542825	0.584281454	0.554296191	0.584281488	0.554296191
−1.24657	0.5639733	-	0.574525263	0.564003924	0.574525624	0.564009932

As shown in Figures 3 and 4, it can be seen that for $\alpha_c \leq \alpha < 0$, dual solutions exist, and it will ultimately end at a critical point α_c. α_c is the key to understand the flow's separating process and solution is not supposed to appear when $\alpha < \alpha_c$. The figures are visualized to show the connection between stretching and shrinking parameter α, when parameters M and ϕ_2 vary with the skin friction coefficient $C_f Re_x^{\frac{1}{2}}$, local Nusselt number $Nu_x Re_x^{-\frac{1}{2}}$, and entropy generation $N_G Re^{-1}$.

Figure 3 shows that the growth of M increases the value of skin friction, decreases the value of the Nusselt number, and raises the value of entropy. M speeds up the fluid's velocity, which upsurges the shear stress, thereby the skin friction value is also escalated. The main reason for this is that the boost in the magnetic force enhances the Lorentz force, which, in turn, resists the movement in the vicinity of the boundary layer, which, as a result, raises the surface friction forces next to the boundary layer. These forces dwindle somewhat when they are far from the layer into the hybrid nanofluid. The local Nusselt number denotes the rate of heat transfer. Hence, depletion of the Nusselt number means the rate of heat transfer also diminishes as M gets bigger. It has been proved that augmenting the magnetic field M accelerates the system's entropy. As a result of swelling the Lorentz force, the temperature of the internal molecules in the liquid is boosted, which in turn grows the energy stored internally by the molecules that make up the hybrid nano liquid causing a contraction in the heat transference from the inside of the fluid to the outside in the conventional heat transfer procedures. This occurrence, in turn, enhances the entropy generation in the thermal system for the hybrid nano liquid. In other words, the drag force caused by the magnetic field generates a lot of friction, enhancing the entropy generation of the system. As the value of M grows, the critical value lessens, such that $\alpha_c = -1.373549$ ($M = 0.065$), $\alpha_c = -1.37818$ ($M = 0.07$), and $\alpha_c = -1.405973$ ($M = 0.1$). Theoretically, when the critical value is lowered, it delays the separation of the boundary layer.

Figure 4 displays the increment effects of GO concentration ϕ_2. As the value of ϕ_2 becomes more concentrated, the critical importance moves toward positive value, such that $\alpha_c = -1.405973$ ($\phi_2 = 0.01$), $\alpha_c = -1.4035$ ($\phi_2 = 0.04$), and $\alpha_c = -1.40035$ ($\phi_2 = 0.08$). When the value of critical value increases, it fastens the separation of the boundary layer. Skin friction coefficient surges because more resistance is built in the fluid, which enlarges the shear stress. Physically, the rise of graphene oxide nano molecules exceeds the collision forces between the molecules inside the nano liquid within the boundary layer, which generates higher surface frictions, which, in turn, accretions the shear stress of the system. The temperature of the fluid is boosted along with the concentration of GO, depicting that more heat is absorbed into the liquid. Hence, the rate of heat transfer into the surface of the system is diminished. The soaring of ϕ_2 does not aid in the rise of disturbance in the system, as the entropy generation reduces when ϕ_2 rises. The boosting in the concentricity of graphene oxide nanoparticles raises the collisions and thus raises the values of the internally stored energy of the particles inside the nano liquid with the swell of these collisions due to the lack of interfacial spaces filled by the graphene oxide nanoparticles, which raises the temperature and thus reduces the generated entropy within the studied thermal system.

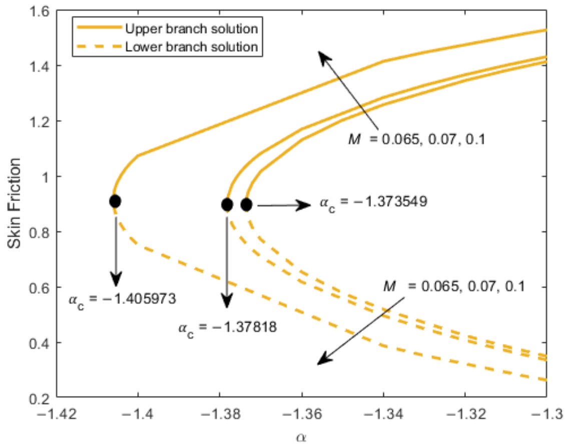

(**a**)

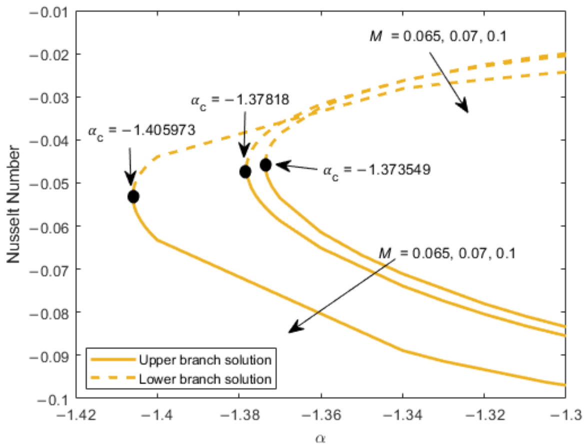

(**b**)

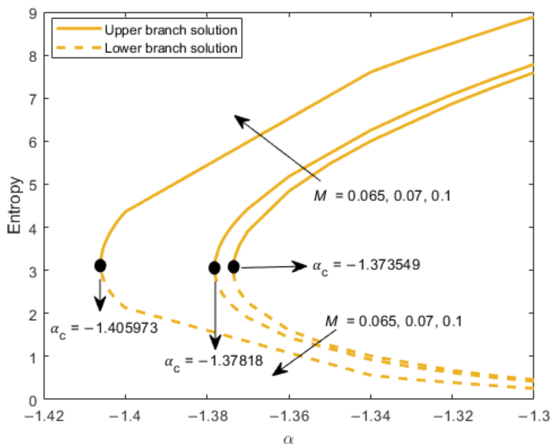

(**c**)

Figure 3. (**a**) Skin friction $C_f Re_x^{1/2}$ for varied M; (**b**) the Nusselt number $Nu_x Re_x^{-1/2}$ for varied M; (**c**) entropy generation $N_G Re^{-1}$ for varied M and $\chi = 0.1$, $\varsigma = 0.1$, $Rd = 0.1$, $Ec = 0.01$, $\epsilon = 0.1$, $Bi = 0.1$.

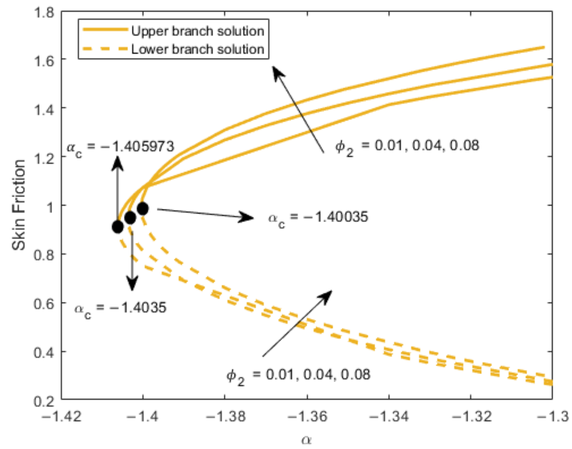

(**a**)

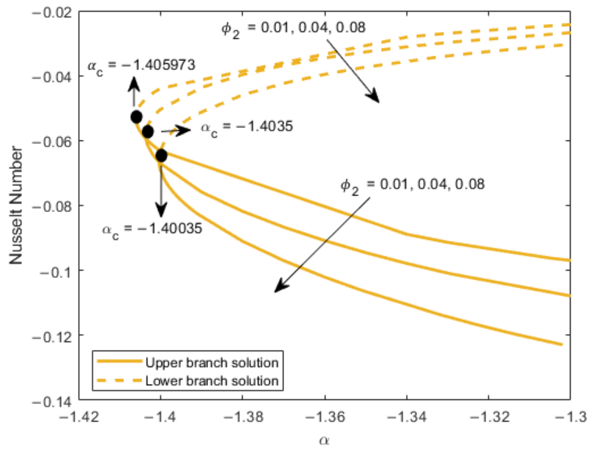

(**b**)

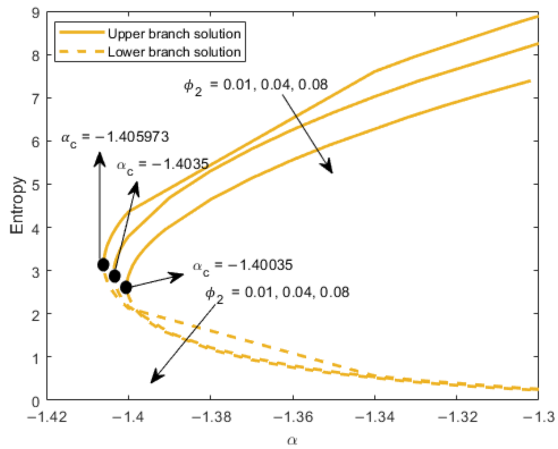

(**c**)

Figure 4. (**a**) Skin friction $C_f Re_x^{1/2}$ for varied ϕ_2; (**b**) the Nusselt number $Nu_x Re_x^{-1/2}$ for varied ϕ_2; (**c**) entropy generation $N_G Re^{-1}$ for varied ϕ_2 and $\mathrm{M} = 0.1$, $\chi = 0.1$, $\varsigma = 0.1$, $Rd = 0.1$, $Ec = 0.01$, $\epsilon = 0.1$, $Bi = 0.1$.

Table 4 displays the values of physical quantities with various values of parameter effects. As the value of velocity slip ϵ builds up, skin friction will be increased. A high viscosity level of GO-Fe_2O_4/EG drives ϵ to increase skin friction. Velocity slip also helps in boosting heat transfer because, as shown in the table, the Nusselt number's value increases when ϵ intensifies. In addition, ϵ elevates the production of disturbance in the system if its value increases. The increment in the rapidity slippage causes the molecules that make up the hybrid nano liquid to lose their stored thermal energy and thus lose their temperature near the boundary layer of the surface. This event physically exceeds the surface friction forces and swells the heat transference process next to the boundary layer of the surface. The slight change in skin friction coefficient, concerning parameter effects Eckert number Ec and thermal radiation Rd, is because these parameters do not affect the momentum of fluid. Instead, the change in the value of the local Nusselt number is evident because these effects are closely related to the temperature of the liquid. Table 4 shows that as the value of Ec increases, the value of the Nusselt number decreases because Ec will prevent the heat from being transferred to the surface. However, when Rd enhances, more heat is carried in the flow, so the value of the Nusselt number will improve. This phenomenon implies that Ec prevents heat transmission while Rd supports the transfer of heat. Noticeably, the strengthening of Ec leads to the increment of entropy. In contrast, when the value of Rd augments, there is a minimal reduction in the entropy generation. It is important to know the behavior of entropy for shrinking surfaces as, based on Adesanya et al. [57], the entropy generation must be regulated for sustainable and efficient manufacturing. For the Biot parameter Bi, the results show that it does not have any effect on all three values of skin friction coefficient, local Nusselt number, and entropy generation. The physical reasons are that when the Eckert number exceeds the required value, the temperature differences of the fluid diminish, meaning that the temperature gradient gradually dwindles, which, in turn, reduces the heat transference rate of the hybrid nano liquid. While the relatively high thermal radiative value reduces the conventional liquid pair and raises the interfacial distances between its molecules, the molecules begin to lose the internally stored thermal energy, and thus the total heat transition rate of the hybrid nano liquid increases.

Table 4. Skin friction coefficient, local Nusselt number, and entropy generation, when $\alpha = -1.4$.

Ec	Rd	ϵ	Bi	$C_f Re_x^{\frac{1}{2}}$		$Nu_x Re_x^{-\frac{1}{2}}$		Entropy	
				1st Solution	2nd Solution	1st Solution	2nd Solution	1st Solution	2nd Solution
0.01	0.1	0.1	0.1	1.072133669	0.750354986	−0.063235727	−0.043932841	4.359617604	2.129891634
0.8	-	-	-	1.072133757	0.750354987	−5.05888402	−3.514627291	26.322070129	12.730478987
1.0	-	-	-	1.072133758	0.750354987	−6.323605114	−4.393284109	38.677880812	18.694241172
-	0.07	-	-	1.072133679	0.750354989	−0.072036548	−0.049763586	4.360764374	2.130420151
-	0.08	-	-	1.072133680	0.750354987	−0.068565825	−0.047457329	4.360295382	2.130203896
-	-	0.2	-	1.612105529	0.466433063	−0.099002297	−0.031028763	9.921324931	0.821946760
-	-	0.3	-	1.816822281	0.370772639	−0.027679856	−0.027591472	12.630987007	0.519323731
-	-	-	0.45	1.072133668	0.750354989	−0.063235889	−0.043932852	4.359617616	2.129891649
-	-	-	0.5	1.072133668	0.750354987	−0.063235894	−0.043932843	4.359617616	2.129891638

The impact of magnetic field M on velocity and temperature profiles at contracting surface $\alpha = -1.3$ is shown in Figure 5. It can be deduced that as M is amplified, the velocity of the liquid elevates, and the momentum boundary layer thickness diminishes. Owing to the presence of radiation parameters and shrinking surface, as the magnetic field increases, the velocity of fluid also increases. Production of Lorentz force caused by the magnetic field interaction with nanofluid that conducts electricity helps fluid particles to move more quickly instead of suppressing the fluid's movement. This occurrence is only possible because the force exerted is directly proportional to the liquid's magnetic field and velocity. The temperature of the fluid, as M increases, goes up little by little at first, but then falls approximately at $\eta = 2$. Before it falls, the temperature accelerates because of the Lorentz force's resistance to the flow, which enhances the heat. After this particular point, as M grows, the temperature of fluid slowly diminishes.

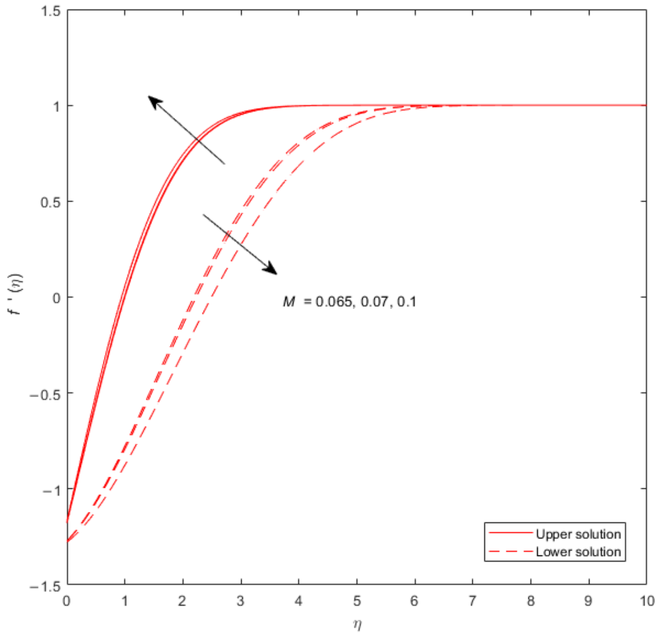

(**a**)

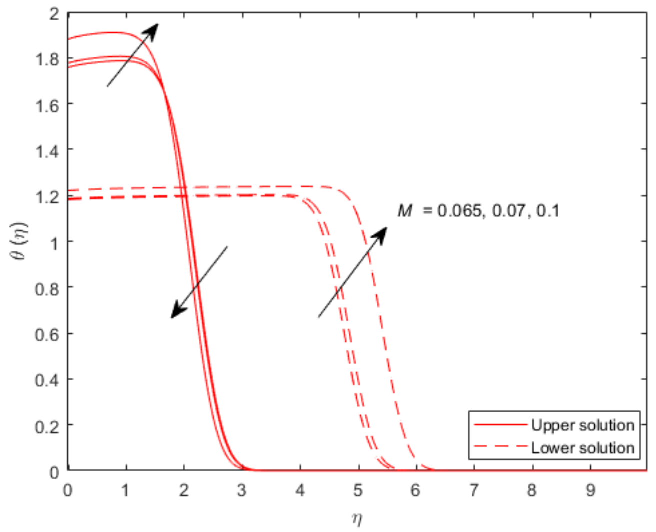

(**b**)

Figure 5. (**a**) $f'(n)$ for varied M; (**b**) $\theta(n)$ for varied M and $\chi = 0.1$, $\varsigma = 0.1$, $Rd = 0.1$, $Ec = 0.01$, $\epsilon = 0.1$, $Bi = 0.1$, $\alpha = -1.3$.

Figure 6 depicts the effects of velocity slip ϵ on the flow of GO-Fe_2O_4/EG fluid at contracting surface $\alpha = -1.4$. It is evident that ϵ increases the velocity of fluid as ϵ increases. A reference to Stoke's Law is needed to clarify this condition, where ϵ will increase if the density of the fluid is higher leading to a higher velocity gap between the liquid and the surface. ϵ is also expected to create an extra interruption and speed up the fluid's velocity. The temperature of the liquid decreases as ϵ goes higher, and as the temperature of the fluid drops, its viscosity climbs. This spectacle leads to a reduction in the boundary layer thickness. This incident is physically due to the fact that the rate of rapidity slippage inside the liquid is inversely proportional to the root of the viscosity of the conventional liquid, which leads to the occurrence of that physical phenomenon that causes the effects mentioned above.

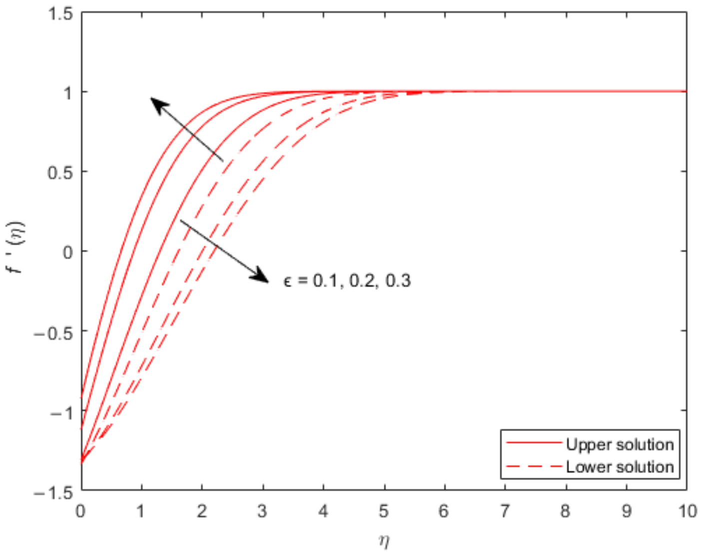

(a)

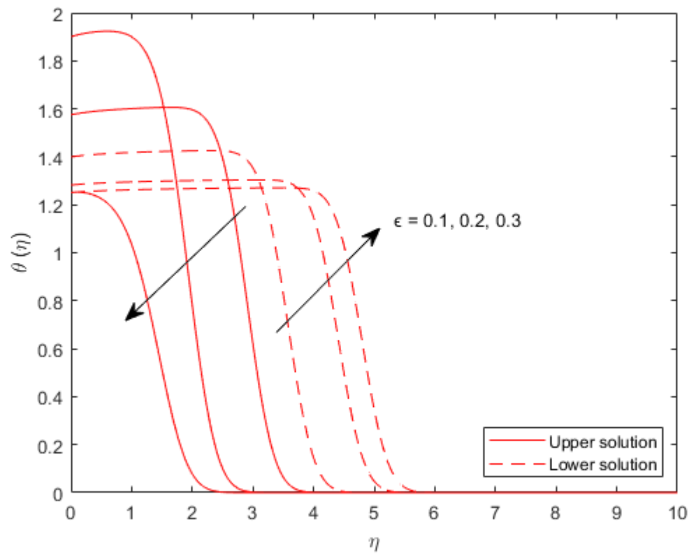

(b)

Figure 6. (**a**) $f'(n)$ for varied ϵ; (**b**) $\theta(n)$ for varied ϵ and $\chi = 0.1$, $\varsigma = 0.1$, $Rd = 0.1$, $Ec = 0.01$, $M = 0.1$, $Bi = 0.1$, $\alpha = -1.4$.

Figure 7 illustrates how the enhancement of graphene oxide's concentration ϕ_2 affects the fluid. The speed of the liquid becomes slower because the concentration escalates the fluid's viscosity and produces more resistance in the flow, which leads to a boundary layer with thicker momentum. However, the temperature of the fluid surges with the value of concentration. It is proven that as ϕ_2 increases, the high thermal conductivity of graphene oxide helps more heat to transmit into the flow and widen the thermal boundary layer. Swelling the graphene oxide nanoparticles rises the total density of the molecules inside the fluid, which reduces the distances between the molecules and between each other, and this negatively affects the movement of the nanofluid and increases the volume of internal collisions. This causes these molecules to lose their thermal energy, which increases the concentration and leads to an increment in the thermal transfer rate of the nano liquid.

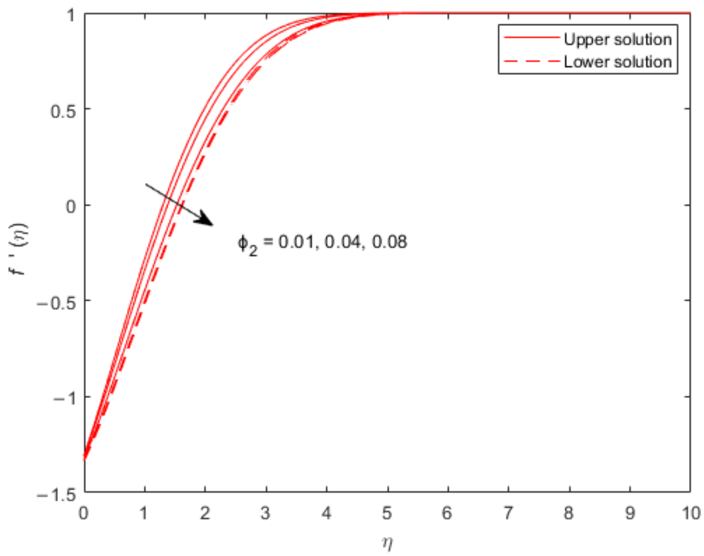

(a)

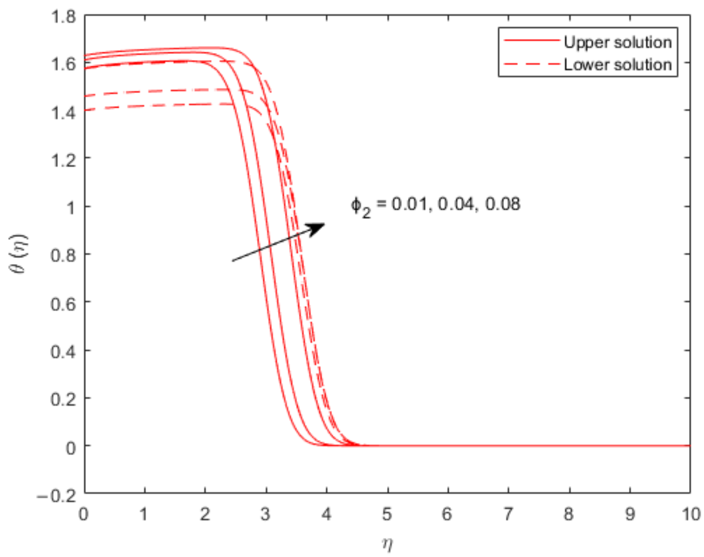

(b)

Figure 7. (**a**) $f'(n)$ for varied ϕ_2; (**b**) $\theta(n)$ for varied ϕ_2 and $M = 0.1$, $\chi = 0.1$, $\varsigma = 0.1$, $Rd = 0.1$, $Ec = 0.01$, $\epsilon = 0.1$, $Bi = 0.1$, $\alpha = -1.4$.

The thermal radiation Rd effect on the temperature of the fluid is analyzed in Figure 8. It is shown in the temperature profile that there exists a turning point near $\eta = 3$. Before the cross-over, the temperature of the liquid gets colder as radiation is enhanced, but after that point, the temperature begins to become hotter. In a sense, it increases because more substantial heat flux is generated due to the enhancement of kinetic energy that results from interparticle collisions. With high radiation, it means that the system is getting hotter. After $\eta = 3$, the thermal profile thickness is boosted. This phenomenon has been referred previously because the energy of the internal molecules changes with the increase in thermal radiative quantity, and the influence occurs on the temperature outlines and thus the rates of heat transition affect in the opposite direction on the rates of generated entropy. This phenomenon appears to be more evident, of course, by approaching the boundary layer of the liquid and less by moving away from it.

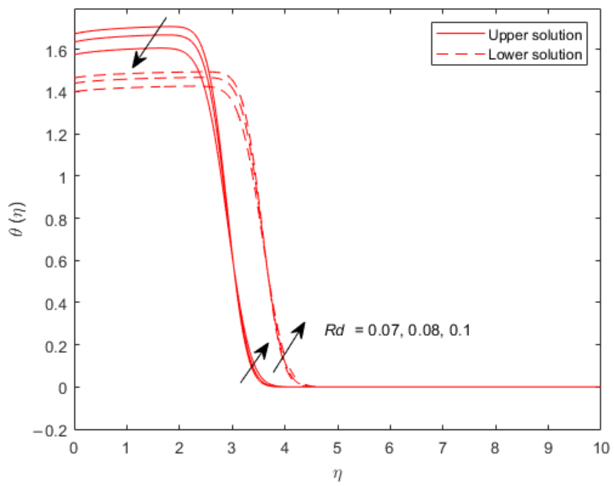

Figure 8. $\theta(n)$ for varied Rd and $M = 0.1$, $\chi = 0.1$, $\varsigma = 0.1$, $Ec = 0.01$, $\epsilon = 0.1$, $Bi = 0.1$, $\alpha = -1.4$.

As illustrated in Figure 9, as Eckert number Ec intensifies, it further increases the liquid's temperature. The strong Ec emphasizes enormous kinetic energy, which means that the temperature will increase due to the heating of the floor. Ec is the proportion of kinetic energy to the total heat present in the thermodynamic system, where the pressure is constant, which explains why high Ec means high kinetic energy. The thermal boundary layer thickens as Ec varies increasingly. As the quantity of Eckert rises, the internal viscosity of the liquid diminishes, so the kinetic energy of the molecules increases, which raises the thermal energy stored in the molecules. As a result, its temperature increases near the surface, then decreases rapidly by moving away from it, passing through the molecules inside the nano liquid.

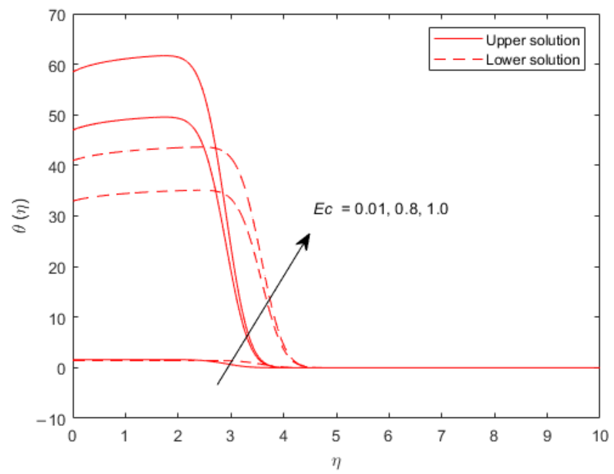

Figure 9. $\theta(n)$ for varied Ec and $M = 0.1$, $\chi = 0.1$, $\varsigma = 0.1$, $Rd = 0.1$, $\epsilon = 0.1$, $Bi = 0.1$, $\alpha = -1.4$.

The effect of Biot number Bi on the thermal profile is presented in Figure 10. It is shown that as the Biot value increases, the temperature of GO-Fe_2O_4/EG and the thickness of the thermal boundary layer decrease. The massive size of the Biot number is said to activate the cooling process on the system's surface, hence cooling down the particles. So, this implies that with the presence of graphene oxide particles in the fluid, Bi enhances the heat diffusivity from the liquid to the surface. The opposite of the physical effect occurs with the Eckert quantity. The role of viscosity increases with the boost in the Biot number near the boundary layer, so the apparent diminishing in temperatures occurs as a result of the increment in heat transition rates approaching this layer, so its thermal thickness rises, and its stored thermal energy is lost. Temperatures begin to decrease until relative stability occurs in the internal viscosity of the nano liquid, at which the temperature stabilizes away from the boundary layer.

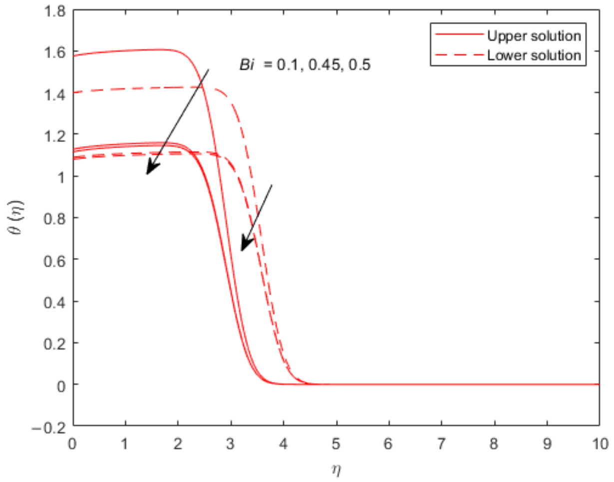

Figure 10. $\theta(\eta)$ for varied Bi and $M = 0.1$, $\chi = 0.1$, $\varsigma = 0.1$, $Rd = 0.1$, $Ec = 0.01$, $\epsilon = 0.1$, $\alpha = -1.4$.

5. Conclusions

The study of a non-Newtonian hybrid nanofluid on a shrinking plate has been analyzed in the presence of MHD and radiation. The mathematical modelling is being dealt with bvp4c to obtain the dual solutions. By utilizing the stability analysis, it was discovered that the upper branch solution is the one that converges instead of the lower branch solution. The results of the current work are as follows:

1. The fluid velocity will be faster in the range of 9.7–54.3% when the values of magnetic field and slip velocity parameters are optimized for the studied values of these parameters.
2. The temperature of the fluid will be hotter by a percentage ranging between 76.6% and 215% with the increment in the value of the thermal radiation parameter effect, the Eckert number, and the concentration of GO, within the limits of the selected values for the parameters under study.
3. Skin friction will be elevated with the high magnetic field, velocity slip, and concentration of GO between 13.7% and 66.5% with these parameters' values incrementations.
4. Thermal radiation and velocity slip can be enhanced to improve the heat transfer rate with the range of 99.8–147% for taken parameters' range.
5. Magnetic field, velocity slip, and Eckert number support the production of entropy (with 16.6–43.9%) when their values are raised within the range for these parameters.

Through many previous studies, it has been proven that the hybrid nanofluid is very useful in improving the efficiency of many applications in various industrial fields by enhancing its heat transfer. Especially in this work, it has been shown that enhancing the concentration of graphene oxide leads to a significant improvement in the rate of heat transfer. Therefore, it is very useful to apply it in the industrial applications, especially in the manufacturing of solar energy systems. This study can also be implemented and extended experimentally in practical life applications in cooperation with chemistry and materials science scientists.

Author Contributions: N.A.A.M.N., A.I. and I.P. formulated the problems. N.A.A. and M.R.E. calculated and solved the problems. N.A.A.M.N., W.J. and M.R.E. inspected the outcomes. All authors have read and agreed to the published version of the manuscript.

Funding: This research was funded by the Ministry of Higher Education Malaysia, Fundamental Research Grant Scheme, grant number FRGS/1/2021/STG06/UPNM/02/1. The APC was funded by National Defence University of Malaysia.

Data Availability Statement: All data generated or analyzed during this study are included in this article.

Acknowledgments: The authors would like to thank Ministry of Higher Education Malaysia and National Defence University of Malaysia for supporting this research.

Conflicts of Interest: The authors declare no conflict of interest. The funders had no role in the design of the study; in the collection, analyses, or interpretation of data; in the writing of the manuscript; or in the decision to publish the results.

Nomenclatures

Bi	Biot number	T_w	the fluid temperature of the surface
B_r	Brinkman number	T_∞	ambient temperature
C_f	skin friction coefficient	b	initial stretching rate
C_p	specific heat $\left(J\ kg^{-1}\ K^{-1}\right)$		Greek symbols
Ec	Eckert number	ϕ	the volume fraction of the nanoparticles
E_G	dimensional entropy (J/K)	ρ	density $Kg\ m^{-3}$
h_f	heat transfer coefficient	σ^*	Stefan Boltzmann constant
k	thermal conductivity $\left(W\ m^{-1}\ K^{-1}\right)$	ψ	stream function
k^*	absorption coefficient	ϵ	velocity slip parameter
Rd	radiation parameter	μ	dynamic viscosity of the fluid $(kgm^{-1}s^{-1})$
N_G	dimensionless entropy generation	ν	kinematic viscosity of the fluid (m^2s^{-1})
Nu_x	local Nusselt number	θ	dimensionless temperature
Pr	Prandtl number (ν/α)	χ, ς	material parameters
q_r	radiative heat flux	α	stretching and shrinking parameter
q_w	wall heat flux		Subscripts
Re	Reynolds number	f	base fluid
v	velocity component $\left(m\ s^{-1}\right)$	0	surface
U_w	the velocity of the stretching sheet	nf	nanofluid
v_w	mass flux constant velocity	s	particles
x, y	dimensional space coordinates (m)	GO	graphene oxide nanoparticle
T	fluid temperature	Fe_2O_4	iron dioxide nanoparticle
M	magnetic parameter	EG	ethylene glycol

References

1. Ramzan, M.; Dawar, A.; Saeed, A.; Kumam, P.; Watthayu, W.; Kumam, W. Heat transfer analysis of the mixed convective flow of magnetohydrodynamic hybrid nanofluid past a stretching sheet with velocity and thermal slip conditions. *PLoS ONE* **2021**, *16*, e0260854. [CrossRef]
2. Hafeez, A.; Yasir, M.; Khan, M.; Malik, M.Y.; Alqahtani, A.S. Buoyancy effect on the chemically reactive flow of Cross nanofluid over a shrinking surface: Dual solution. *Int. Commun. Heat Mass Transf.* **2021**, *126*, 105438. [CrossRef]
3. Othman, M.N.; Jedi, A.; Bakar, N.A.A. MHD Flow and Heat Transfer of Hybrid Nanofluid over an Exponentially Shrinking Surface with Heat Source/Sink. *Appl. Sci.* **2021**, *11*, 8199. [CrossRef]
4. Parvin, S.; Isa, S.S.P.M.; Arifin, N.M.; Ali, F.M.A. The Inclined Factors of Magnetic Field and Shrinking Sheet in Casson Fluid Flow, Heat and Mass Transfer. *Symmetry* **2021**, *13*, 373. [CrossRef]
5. Lund, L.A.; Omar, Z.; Dero, S.; Khan, I.; Baleanu, D.; Nisar, K.S. Magnetized Flow of Cu + Al_2O_3 + H_2O Hybrid Nanofluid in Porous Medium: Analysis of Duality and Stability. *Symmetry* **2020**, *12*, 1513. [CrossRef]
6. Yasir, M.; Hafeez, A.; Khan, M. Thermal conductivity performance in hybrid (SWCNTs-CuO/Ethylene glycol) nanofluid flow: Dual solutions. *Ain Shams Eng. J.* **2022**, *13*, 101703. [CrossRef]
7. Jawad, M.; Jan, R.; Boulaaras, S.; Amin, I.; Shah, N.A.; Idris, S.A. Unsteady Electrohydrodynamic Stagnation Point Flow of Hybrid Nanofluid Past a Convective Heated Stretch/Shrink Sheet. *Adv. Math. Phys.* **2021**, *2021*, 6229706. [CrossRef]
8. Khan, A.A.; Zaimi, K.; Ying, T.Y. Unsteady MHD Stagnation Point Flow of Al_2O_3-Cu/H_2O Hybrid Nanofluid Past a Convectively Heated Permeable Stretching/Shrinking Sheet with Suction/Injection. *J. Adv. Res. Fluid Mech. Therm. Sci.* **2022**, *96*, 96–114. [CrossRef]
9. Rahman, A.N.H.; Bachok, N.; Rosali, H. Numerical Solutions of MHD Stagnation-Point Flow over an Exponentially Stretching/Shrinking Sheet in a Nanofluid. In Proceedings of the 2nd International Conference on Applied & Industrial Mathematics and Statistics, Kuantan, Malaysia, 23–25 July 2019.
10. Rao, D.P.C.; Thiagarajan, S.; Kumar, V.S. Heat transfer in darcy-forcheimer flow of tangent hyperbolic fluid over an inclined plate with joule heating. *J. Appl. Math. Comput. Mech.* **2021**, *20*, 31–40. [CrossRef]

11. Venkatesan, G.; Reddy, A.S. Insight into the dynamics of blood conveying alumina nanoparticles subject to Lorentz force, viscous dissipation, thermal radiation, Joule heating, and heat source. *Eur. Phys. J. Spec. Top.* **2021**, *230*, 1475–1485. [CrossRef]
12. Gholinia, M.; Hoseini, M.E.; Gholinia, S. A numerical investigation of free convection MHD flow of Walters-B nanofluid over an inclined stretching sheet under the impact of Joule heating. *Therm. Sci. Eng. Prog.* **2019**, *11*, 272–282. [CrossRef]
13. Alaidrous, A.A.; Eid, M.R. 3-D electromagnetic radiative non-Newtonian nanofluid flow with Joule heating and higher-order reactions in porous materials. *Sci. Rep.* **2020**, *10*, 14513. [CrossRef] [PubMed]
14. Jangid, S.; Alessa, N.; Mehta, R.; Thamaraikannan, N.; Shilpa, S. Numerical Study of Cattaneo–Christov Heat Flux on Water-Based Carreau Fluid Flow over an Inclined Shrinking Sheet with Ternary Nanoparticles. *Symmetry* **2022**, *14*, 2605. [CrossRef]
15. Ferdows, M.; Zaimi, K.; Rashad, A.M.; Nabwey, H.A. MHD Bioconvection Flow and Heat Transfer of Nanofluid through an Exponentially Stretchable Sheet. *Symmetry* **2020**, *12*, 692. [CrossRef]
16. Bazdar, H.; Toghraie, D.; Pourfattah, F.; Akbari, O.A.; Nguyen, H.M.; Asadi, A. Numerical investigation of turbulent flow and heat transfer of nanofluid inside a wavy microchannel with different wavelengths. *J. Therm. Anal. Calorim.* **2020**, *139*, 2365–2380. [CrossRef]
17. Arasteh, H.; Mashayekhi, R.; Goodarzi, M.; Motaharpour, S.H.; Dahari, M.; Toghraie, D. Heat and fluid flow analysis of metal foam embedded in a double layered sinusoidal heat sink under local thermal non-equilibrium condition using nanofluid. *J. Therm. Anal. Calorim.* **2019**, *138*, 1461–1476. [CrossRef]
18. Qureshi, M.A. A case study of MHD driven Prandtl-Eyring hybrid nanofluid flow over a stretching sheet with thermal jump conditions. *Case Stud. Therm. Eng.* **2021**, *28*, 101581. [CrossRef]
19. Mashayekhi, R.; Khodabandeh, E.; Akbari, O.A.; Toghraie, D.; Bahiraei, M.; Gholami, M. CFD analysis of thermal and hydrodynamic characteristics of hybrid nanofluid in a new designed sinusoidal double-layered microchannel heat sink. *J. Therm. Anal. Calorim.* **2018**, *134*, 2305–2315. [CrossRef]
20. Hussain, Z.; Muhammad, S.; Anwar, M.S. Effects of first-order chemical reaction and melting heat on hybrid nanoliquid flow over a nonlinear stretched curved surface with shape factors. *Adv. Mech. Eng.* **2021**, *13*. [CrossRef]
21. Masood, S.; Farooq, M. Influence of thermal stratification and thermal radiation on graphene oxide Ag/H2O hybrid nanofluid. *J. Therm. Anal. Calorim.* **2021**, *143*, 1361–1370. [CrossRef]
22. Ahmad, S.; Ali, K.; Ashraf, M.; Khalifa, H.A.E.W.; ElSeabee, F.A.A.; Tag El Din, E.S.M. Analysis of pure nanofluid (GO/engine oil) and hybrid nanofluid (GO–Fe_3O_4/engine oil): Novel thermal and magnetic features. *Nanotechnol. Rev.* **2022**, *11*, 2903–2915. [CrossRef]
23. Muhammad, N.; Nadeem, S. Ferrite nanoparticles Ni- $ZnFe_2O_4$, Mn- $ZnFe_2O_4$ and Fe_2O_4 in the flow of ferromagnetic nanofluid. *Eur. Phys. J. Plus* **2017**, *132*, 377. [CrossRef]
24. Ramzan, M.; Gul, N.; Chung, J.D. Numerical treatment of radiative Nickel–Zinc ferrite-Ethylene glycol nanofluid flow past a curved surface with thermal stratification and slip conditions. *Sci. Rep.* **2020**, *10*, 16832. [CrossRef]
25. Tahir, H.; Khan, U.; Din, A.; Chu, Y.M.; Muhammad, N.; Li, X.M. Hybridized two phase ferromagnetic nanofluid with $NiZnFe_2O_4$ and $MnZnFe_2O_4$. *Ain Shams Eng. J.* **2021**, *12*, 3063–3070. [CrossRef]
26. Muhammad, T.; Waqas, H.; Khan, S.A.; Ellahi, R.; Sait, S.M. Significance of nonlinear thermal radiation in 3D Eyring–Powell nanofluid flow with Arrhenius activation energy. *J. Therm. Anal. Calorim.* **2021**, *143*, 929–944. [CrossRef]
27. Powell, R.E.; Eyring, H. Mechanisms for the relaxation theory of viscosity. *Nature* **1944**, *154*, 427–428. [CrossRef]
28. Akbar, N.S.; Ebaid, A.; Khan, Z.H. Numerical analysis of magnetic field effects on Eyring–Powell fluid flow towards a stretching sheet. *J. Magn. Magn. Mater.* **2015**, *382*, 355–358. [CrossRef]
29. Ogunseye, H.A.; Tijani, Y.O.; Sibanda, P. Entropy generation in an unsteady Eyring-Powell hybrid nanofluid flow over a permeable surface: A Lie group analysis. *Heat Transf.* **2020**, *49*, 3374–3390. [CrossRef]
30. Manvi, B.; Tawade, J.; Biradar, M.; Noeiaghdam, S.; Gamiz, U.F.; Govindan, V. The effects of MHD radiating and non-uniform heat source/sink with heating on the momentum and heat transfer of Eyring-Powell fluid over a stretching. *Results Eng.* **2022**, *14*, 100435. [CrossRef]
31. Hamida, M.B.B.; Charrada, K. Heat Generation/Absorption Effect on Natural Convection Heat Transfer in a Square Enclosure Filled with a Ethylene Glycol-Copper Nanofluid Under Magnetic Field. *Am. J. Mod. Energy* **2015**, *1*, 1–16. [CrossRef]
32. Kumar, T.S. Hybrid nanofluid slip flow and heat transfer over a stretching surface. *Partial. Differ. Equ. Appl. Math.* **2021**, *4*, 100070. [CrossRef]
33. Ahmad, S.; Nadeem, S.; Rehman, A. Mathematical Analysis of Thermal Energy Distribution in a Hybridized Mixed Convective Flow. *J. Nanofluids* **2021**, *10*, 222–231. [CrossRef]
34. Roja, A. Scrutinization of entropy on MHD Eyring–Powell C71500–Ti6Al4V nanoparticles suspended in a $C_2H_6O_2-H_2O$ hybrid base fluid with heat generation. *Heat Transf.* **2021**, *51*, 193–209. [CrossRef]
35. Rashad, A.M.; Nafe, M.A.; Eisa, D.A. Heat Generation and Thermal Radiation Impacts on Flow of Magnetic Eyring–Powell Hybrid Nanofluid in a Porous Medium. *Arab. J. Sci. Eng.* **2022**, *48*, 939–952. [CrossRef]
36. Mostafazadeh, A.; Toghraie, D.; Mashayekhi, R.; Akbari, O.A. Effect of radiation on laminar natural convection of nanofluid in a vertical channel with single- and two-phase approaches. *J. Therm. Anal. Calorim.* **2019**, *138*, 779–794. [CrossRef]
37. Dogonchi, A.S.; Divsalar, K.; Ganji, D.D. Flow and heat transfer of MHD nanofluid between parallel plates in the presence of thermal radiation. *Comput. Methods Appl. Mech. Eng.* **2016**, *310*, 58–76. [CrossRef]

38. Dogonchi, A.S.; Alizadeh, M.; Ganji, D.D. Investigation of MHD Go-water nanofluid flow and heat transfer in a porous channel in the presence of thermal radiation effect. *Powder Technol.* **2017**, *28*, 1815–1825. [CrossRef]
39. Ashwinkumar, G.P.; Samrat, S.P.; Sandeep, N. Convective heat transfer in MHD hybrid nanofluid flow over two different geometries. *Int. Commun. Heat Mass Transf.* **2021**, *127*, 105563. [CrossRef]
40. Shoaib, M.; Raja, M.A.Z.; Sabir, M.T.; Islam, S.; Shah, Z.; Kumam, P.; Alrabaiah, H. Numerical investigation for rotating flow of MHD hybrid nanofluid with thermal radiation over a stretching sheet. *Sci. Rep.* **2020**, *10*, 18533. [CrossRef]
41. Yahya, A.U.; Salamat, N.; Huang, W.H.; Siddique, I.; Abdal, S.; Hussain, S. Thermal characteristics for the flow of Williamson hybrid nanofluid (MoS_2 + ZnO) based with engine oil over a stretched sheet. *Case Stud. Therm. Eng.* **2021**, *26*, 101196. [CrossRef]
42. Das, S.; Sarkar, S.; Jana, R.N. Feature of Entropy Generation in Cu-Al_2O_3/Ethylene Glycol Hybrid Nanofluid Flow Through a Rotating Channel. *Bionanoscience* **2020**, *10*, 950–967. [CrossRef]
43. Sreedevi, P.; Reddy, P.s. Entropy generation and heat transfer analysis of alumina and carbon nanotubes based hybrid nanofluid inside a cavity. *Phys. Scr.* **2021**, *96*, 085210. [CrossRef]
44. Naganthran, K.; Nazar, R.; Siri, Z.; Hashim, I. Entropy Analysis and Melting Heat Transfer in the Carreau Thin Hybrid Nanofluid Film Flow. *Mathematics* **2021**, *9*, 3092. [CrossRef]
45. Mekheimer, K.S.; Abo-Elkhair, R.E.; Ali, K.K.; Keshta, M.G. Entropy generation and curvature effect on peristaltic thrusting of (Cu–Al_2O_3) hybrid nanofluid in resilient channel: Nonlinear analysis. *Heat Transf.* **2021**, *50*, 7918–7948. [CrossRef]
46. Ghali, D.; Redouane, F.; Abdelhak, R.; Mahammed, A.B.; Zineb, C.D.; Jamshed, W.; Eid, M.R.; Eldin, S.M.; Musa, A.; Nasir, N.A.A.M. Mathematical Entropy Analysis of Natural Convection of MWCNT—Fe_3O_4/Water Hybrid Nanofluid with Parallel Magnetic Field via Galerkin Finite Element Process. *Symmetry* **2022**, *14*, 2312. [CrossRef]
47. Hayat, A.U.; Ullah, I.; Khan, H.; Weera, W.; Galal, A.M. Numerical Simulation of Entropy Optimization in Radiative Hybrid Nanofluid Flow in a Variable Features Darcy–Forchheimer Curved Surface. *Symmetry* **2022**, *14*, 2057. [CrossRef]
48. Waini, I.; Ishak, A.; Pop, I. Hybrid nanofluid flow and heat transfer past a vertical thin needle with prescribed surface heat flux. *International Int. J. Numer. Methods Heat Fluid Flow* **2019**, *29*, 4875–4894. [CrossRef]
49. Jamshed, W.; Al-Kouz, W.; Nasir, N.A.A.M. Computational single phase comparative study of inclined MHD in a Powell–Eyring nanofluid. *Heat Transf.* **2021**, *50*, 3879–3912. [CrossRef]
50. Devi, S.P.A.; Devi, S.U. Numerical investigation of hydromagnetic hybrid Cu-Al2O3/water nanofluid flow over a permeable stretching sheet with suction. *Int. J. Nonlinear Sci. Numer. Simul.* **2016**, *17*, 249–257. [CrossRef]
51. Khashi'ie, N.S.; Waini, I.; Kasim, A.R.M.; Zainal, N.A.; Arifin, N.M.; Pop, I. Thermal progress of a non-Newtonian hybrid nanofluid flow on a permeable Riga plate with temporal stability analysis. *Chin. J. Phys.* **2022**, *77*, 279–290. [CrossRef]
52. Kumar, R.N.; Gowda, R.J.P.; Alam, M.M.; Ahmad, I.; Mahrous, Y.M.; Gorji, M.R.; Prasannakumara, B.C. Inspection of convective heat transfer and KKL correlation for simulation of nanofluid flow over a curved stretching sheet. *Int. Commun. Heat Mass Transf.* **2021**, *126*, 105445. [CrossRef]
53. Al-Mubaddel, F.S.; Farooq, U.; Al-Khaled, K.; Hussain, S.; Khan, S.U.; Aijaz, M.O.; Rahimi-Gorji, M.; Waqas, H. Double stratified analysis for bioconvection radiative flow of Sisko nanofluid with generalized heat/mass fluxes. *Phys. Scr.* **2021**, *96*, 055004. [CrossRef]
54. Ganesh, N.V.; Al-Mdallal, Q.M.; Kameswaran, P.K. Numerical study of MHD effective Prandtl number boundary layer flow of γ Al_2O_3 nanofluids past a melting surface. *Case Stud. Therm. Eng.* **2019**, *13*, 100413. [CrossRef]
55. Bachok, N.; Ishak, A.; Pop, I. Melting heat transfer in boundary layer stagnation-point flow towards a stretching/shrinking sheet. *Phys. Lett. A* **2010**, *374*, 4075–4079. [CrossRef]
56. Wahid, N.S.; Arifin, N.M.; Pop, I.; Bachok, N.; Hafidzuddin, M.E.H. MHD stagnation-point flow of nanofluid due to a shrinking sheet with melting, viscous dissipation, and Joule heating effects. *Alex. Eng. J.* **2022**, *61*, 12661–12672. [CrossRef]
57. Adesanya, S.O.; Onanaye, A.S.; Adeyemi, O.G.; Rahimi-Gorji, M.; Alarifi, I.M. Evaluation of heat irreversibility in couple stress falling liquid films along heated inclined substrate. *J. Clean. Prod.* **2019**, *239*, 117608. [CrossRef]